JOURNAL OF GEOPHYSICAL RESEARCH, VOL. 104, NO. B6, PAGES 13,083–13,099, JUNE 10, 1999

Contribution of radar interferometry to a two-step inversion of the kinematic process of the 1992 Landers earthquake

Bruno Hernandez

Institut de Protection et de Sûreté Nucléaire, Fontenay-aux-Roses, France
Laboratoire de Géophysique Interne et Tectonophysique, Université Joseph Fourier, Grenoble, France

Fabrice Cotton

Institut de Protection et de Sûreté Nucléaire, Fontenay-aux-Roses, France

Michel Campillo

Laboratoire de Géophysique Interne et Tectonophysique, Université Joseph Fourier, Grenoble, France
Institut Universitaire de France, France

Abstract. We study the rupture process of the 1992 Landers earthquake. To limit the trade-off between slip amplitude and rupture time that affects solutions using only seismological data, we adopt a two-step approach. We first constrain the slip distribution and its uncertainty by independent geodetic data to recover in the second step the temporal details of the rupture propagation. The first step consists of an inversion of interferometric data and Global Positioning System measurements, both independently and together, to constrain slip distribution on a three-segment fault model along both strike and dip direction. We use a genetic algorithm to test the uniqueness of the solution and a least squares formulation to find the model which best fits the data. We conclude from the results of these geodetic inversions that interferometric data are rich enough to access the slip distribution in the case of the Landers earthquake. Since the surface deformations are more sensitive to shallow slip in our configuration, the slip amplitude is better resolved near the surface than at depth. The resulting slip distribution is in agreement with geological observations at the surface and confirms the heterogeneous nature of the Landers earthquake. Most of the slip occurs at shallow depths, on the Homestead Valley fault (second segment), with a maximum value of around 7 m. Another high slip zone is observed on the Johnson Valley fault (first segment) at 8 km depth. In the second step, we invert strong motion data with the a priori final slip amplitude and its uncertainty deduced from geodetic data to constrain the time history of the rupture process. This second step emphasizes a strong variation of the temporal development of the earthquake. Fast rupture front velocities appear within high slip zones, and the rupture slows when it encounters a resistance along the fault. On average, the rupture front propagates with velocities close to the S wave velocity and terminates about 20 s after initiation. The large variations in both slip amplitude and rupture velocity suggest that the rupture process is better described by successively breaking asperities than by a pulse propagating with constant velocity.

1. Introduction

In seismology, basic problems of initiation, propagation, and healing of the rupture process are still not well understood. Since the near-field strong ground motion records of the Imperial Valley earthquake [*Olson and Apsel*, 1982; *Hartzell and Heaton*, 1983; *Archuleta*, 1984], rupture heterogeneity became evident. This heterogeneity is probably generated by a combination of the static prestress field due to tectonic forces, past seismicity [*Kanamori and Stewart*, 1978], fault geometry [*Scholz*, 1989; *Cotton and Campillo*, 1995], and the effect of the dynamic process governed by friction [*Carlson and Langer*, 1989; *Cochard and Madariaga*, 1994].

In order to understand the main origin of the rupture complexity, seismologists adopt two approaches. On the one hand, forward dynamic models are developed to describe the rupture process [*Das and Kostrov*, 1983; *Mikumo et al.*, 1987; *Heaton*, 1990; *Cochard and Madariaga*, 1994]. On the other hand, near-field strong ground motions are inverted to estimate the slip; the relative displacement of one side of the fault with respect to the other; and the time history of the seismic process. Over the past 2 decades, kinematic models deduced from near-field data have provided insight into the spatial and temporal details of the rupture process for many earthquakes. The rupture models were derived by matching recorded data with theoretical data generated, assuming planar fault surfaces. Recently, attempts have been made to understand the dynamic process from kinematic models

Paper number 1999JB900078.
0148-0227/99/1999JB900078$09.00

[*Quin*, 1990; *Miyatake*, 1992; *Fukuyama and Mikumo*, 1993; *Ide and Takeo*, 1996; *Bouchon*, 1997; *Olsen et al.*, 1997]. In addition to its importance to the study of the source process, the kinematic approach is used to model strong ground motion in seismic hazard.

Despite much research on kinematic models, there remain important discrepancies among rupture inversions of the same earthquake published by different authors. For example, the strong motion inversion of the Landers earthquake leads to different solutions [*Cohee and Beroza*, 1994b; *Wald and Heaton*, 1994; *Cotton and Campillo*, 1995]. These dissimilarities can be caused by the model parameterization, the data weighting, the bandwidth of the wavefield, or the inversion procedure and are often cited as indicative of the amount of uncertainty in rupture models obtained from strong motion data. For the most part, past studies have concentrated on deriving a model that fits the strong motion data, without much emphasis on assessing the solution stability or spatial resolution. Using standard inverse methods, it is not difficult to obtain a solution that matches the data reasonably well [*Cohee and Beroza*, 1994a]. The greater challenge lies in estimating the reliability. The knowledge of the resolution on the kinematic parameters is a result that is as important as the parameters themselves. It is also important to test the uniqueness of the solution.

Another challenge consists in finding rupture front velocities. Recently, the dynamic simulation of the 1992 Landers earthquake performed by *Olsen et al.* [1997] has shown strong variation of the rupture front velocity from subsonic to supersonic values. Such variations are not expected from kinematic inversions. Two reasons can explain why evidence of such variation of the local rupture front velocity is sparse in past inversions of seismic data. First, there is a trade-off between slip and rupture time that affects solutions based on strong motion data alone. Consequently, it is necessary to constrain the slip amplitude distribution by independent data (radar interferometry and other geodetic data) in order to recover the temporal details of the rupture propagation using seismological data (Figure 1). Second, a priori constraints introduced by the parameterization used in the inversions usually constrain the maximum value of the rupture front velocity. Therefore it is necessary to allow temporal parameters to vary freely [*Cotton and Campillo*, 1995; *Hartzell et al.*, 1996].

The June 28, 1992, Landers earthquake is the largest well-recorded earthquake in California to date. In addition to the high quality and variety of classical data, this earthquake provided the first opportunity to apply the technique of synthetic aperture radar (SAR) interferometry to detect coseismic ground displacements [*Massonnet et al.*, 1993]. The interferogram produced by differencing the phase between SAR images taken before (April 24, 1992) and after the earthquake (June 18, 1993) provides a contour map of the component of the surface displacement field parallel to the vector between the ground and the radar remote sensor. Each fringe corresponds to an interval of displacement of 28.3 mm toward the satellite or in the opposite direction (Figure 2). The applications of radar interferometry to changes in Earth's surface are described by *Massonnet and Feigl* [1998].

The main advantage of interferometric data is that they do not use instrumentation on the ground. An interferogram can be the only available near-field measurement of earthquake effects in a poorly instrumented area. This new kind of data makes it possible to have an idea of the focal mechanism [*Feigl et al.*, 1995]. The high spatial density of a radar interferogram also offers the possibility to constrain the location and geometry of active faults to a greater degree than using conventional geodetic or seismic data [*Ozawa et al.*, 1997]. Nevertheless, SAR data have never been used in combination with seismological and other geodetic data to constrain the rupture process.

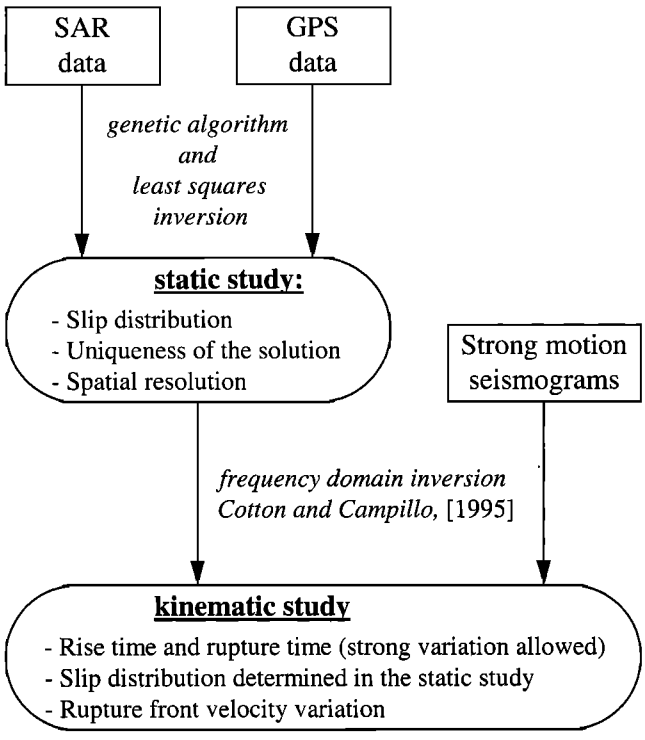

Figure 1. Flow chart of the two-steps source study of the Landers earthquake. GPS and SAR data are used in the static study. Strong motion seismic data are inverted with the a priori slip distribution and its resolution deduced from SAR and GPS combined data.

The questions addressed in this paper are:

Are SAR data alone useful to study the static rupture process ? If GPS and strong motion data are available, is it useful to use interferometric data to improve the solution ? Do strong motion accelerograms combined with interferometric data constrain the temporal growth of the rupture accurately, and is it possible to have more precision on the rupture propagation than using only strong ground motion data ?

To answer these questions, we estimate the rupture process of the 1992 Landers earthquake in two steps from geodetic and seismological data (Figure 1). In the first step, we compute the static solution by inverting the deformation field measured by radar interferometry to constrain the slip distribution on the fault. We use rich SAR data on a well-known earthquake to test our approach. Next, we invert Gobal Positioning System (GPS) measurements alone and also in combination with SAR data. We discuss the resolution obtained by the inversion of the different data sets. We analyze the uniqueness of the solution and the influence of a smoothing constraint.

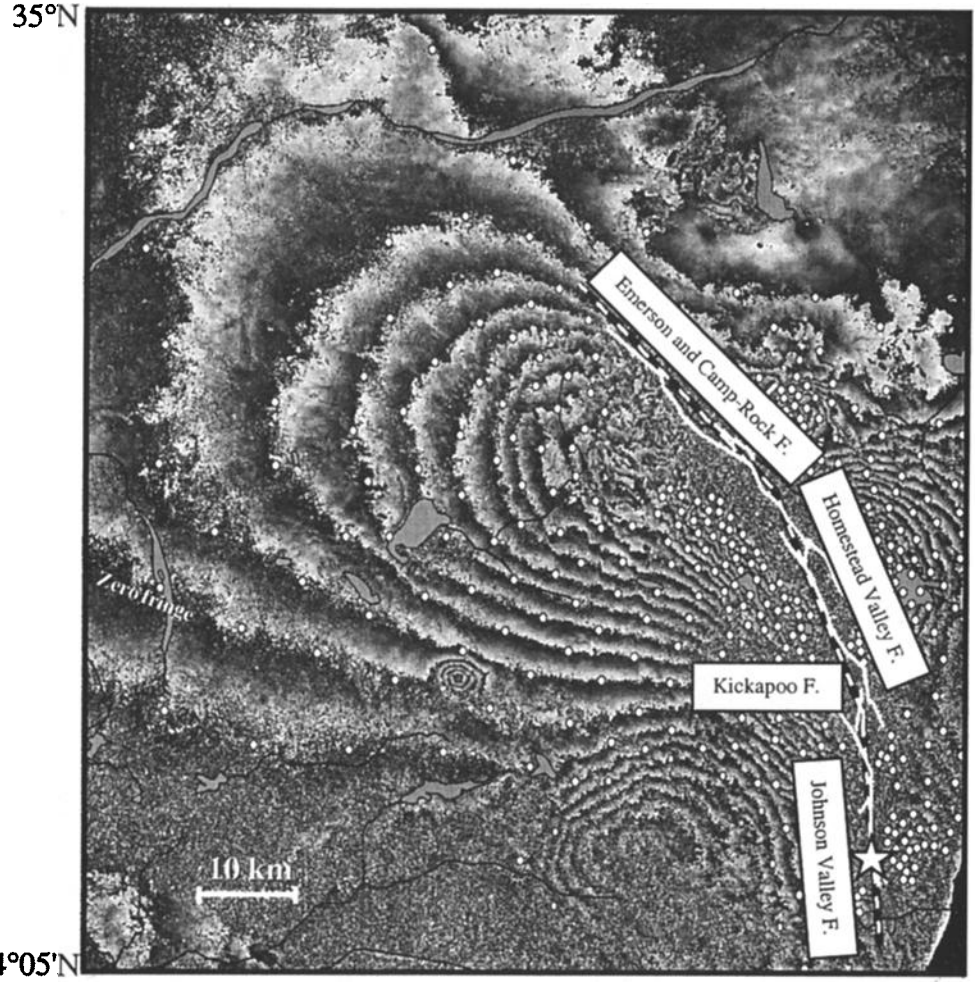

Figure 2. Observed interferogram of the June 28, 1992, Landers earthquake obtained with ERS-1 SAR data [*Massonnet et al.*, 1993]. Fringes are contour lines of equal displacement of the ground along the line of sight of satellite. One full gray-scale cycle represents 28.3 mm of surface displacement in the ground-to-satellite direction between April 24, 1992, and June 18, 1993. The average residual on the measurement is estimated to be no more than one fringe and is mainly due to atmospheric propagation heterogeneity, residual topographic contributions, and hydrographic network (dark lines) perturbations. This map also shows the fault trace offset (white lines) simplified from *Hart et al.* [1993], the epicenter location (star), and the surface projection of the three vertical segments of the model fault (dashed lines). To use a good quality data set, we extract several hundred points from the interferogram where the signal is not perturbed by groundwater content or post seismic deformation due to off fault aftershocks.

In the second step, we study the rupture front velocity variation using strong ground motion data and the static solution and its error deduced from a combination of SAR and GPS data. This two-step inversion (Figure 1) limits the trade-off between parameters and allows the temporal parameter to vary freely over a wide range. The main goal of this second step is to obtain a better knowledge of the kinematic rupture process. We want to know if the rupture front propagates smoothly on the fault, or if, on the contrary, the velocity varies strongly and whether strong variations coincide with the location of asperities and barriers.

2. Geodetic Data

The data set is composed of GPS measurements of displacement [*Hudnut et al.*, 1994] and an interferogram of the Landers earthquake [*Massonnet et al.*, 1994].

The interferogram shows the ground deformation between April 24, 1992, and June 18, 1993. The displacement is extracted at several hundred sites from the image shown in Figure 2. For each data point located on an interferometric fringe, we associate a change in the ground-to-satellite distance assuming zero motion for a fringe far from the fault zone. The location of the zero fringe displacement due to the coseismic slip is well estimated thanks to a forward calculation of the ground deformation using the slip distribution deduced from strong motion inversion [*Cotton and Campillo*, 1995; *Hernandez et al.*, 1997]. The phase values in the interferogram are converted from ambiguous cycles into absolute changes in displacement using a manual unwrapping approach. Each cycle of phase corresponds to an interval of displacement of 28.3 mm in the ground-to-satellite direction. We do not use an automatic unwrapping method because of perturbations mainly due to hydrography and local

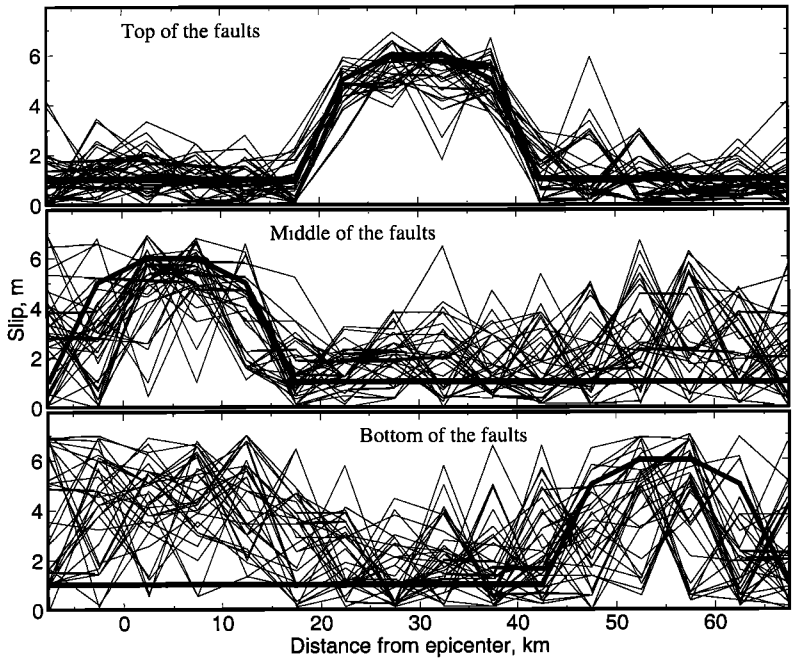

Figure 3. Results from one genetic algorithm inversion of synthetic SAR data calculated from a three-asperity model represented by thick lines. The 50 best models are plotted, and 10^5 models are tested using a population size of 200 and 500 generations. The slip is well constrained in the upper part of the fault, but the resolution decreases with depth.

aftershocks that we do not take into account in our model. The resulting data set consists of 406 triplets containing latitude, longitude, and the static displacement in ground-to-satellite direction. We estimate that the error on the displacement is of the order of one fringe (3 cm).

These SAR data include the static deformation over more than 1 year. The deformation is mainly coseimic: the amplitude of preseismic and postseismic equivalent slip integrated over a period of 14 months is estimated to be no more than a few decimeters [*Hernandez et al.*, 1997]. Post-seismic interferograms of the Landers area [*Massonnet et al.*, 1996; *Peltzer et al.*, 1996], made from images acquired 5 days after the earthquake and later suggest a postseismic slip of several centimeters, comparable to that obtained from an analysis of GPS data [*Blewitt et al.*, 1993; *Shen et al.*, 1994]. Thus the preseismic and postseismic effects can be considered to be minor compared to the deformation field created by the mainshock. Moreover, we do not extract data points near large identified aftershocks not located on the faults that moved during the mainshock.

In our GPS inversion, we used only the horizontal measurements made by *Hudnut et al.* [1994] located in a 100-km-radius area around the fault zone. These surveys provided coseismic displacement data. We do not use GPS vertical measurements because of their large uncertainties.

3. Forward Modeling

For the direct modeling, we follow the frequency domain approach of *Cotton and Campillo* [1995] restricted to the case of zero frequency. We calculate transfer functions for a layered half-space rather than a uniform elastic half-space in order to have a more realistic representation of the crustal deformation [*Savage*, 1998]. The crustal model we use in this study is described by *Campillo and Archuleta* [1993]. We divide the fault that ruptured during the Landers earthquake into three segments: the Johnson Valley fault to the south (strike 355°), where the hypocenter is located, the Homestead Valley fault (strike 339°) in the central part and the Emerson and Camp Rock fault (strike 317°) to the northwest. The fault is modeled by three vertical planes (Figure 2), each divided into discrete 5-km-wide-square subfaults [*Cotton and Campillo*, 1995]. The transfer functions [*Kennett and Kerry*, 1979; *Bouchon*, 1981] are calculated in the ground-to-satellite direction for SAR data and in the horizontal plane for GPS data. The ground deformation D_i at a point i (SAR or GPS data) can be represented as a linear sum of n subfaults contributions:

$$D_i(w=0) = \sum_{k=1}^{n} G_{ki}(w=0)U_k \qquad (1)$$

where G is the transfer matrix of the deformation observed in i for a unit strike slip in k. U_k is the unknown mean slip amplitude of the k^{th} subfault. This simple parameterization, which is consistent with the fault trace observed by geologists (Figure 2) and the aftershocks distribution, limits the number of parameters of the model to 48 unknown slips.

4. Inversion Methods

The inverse problem consists in minimizing the difference between the observed ground deformation and that calculated with the forward modeling. It can be solved using a linear least squares inversion scheme. We assume that the forward problem is exactly solved by the linear equation (1), that the

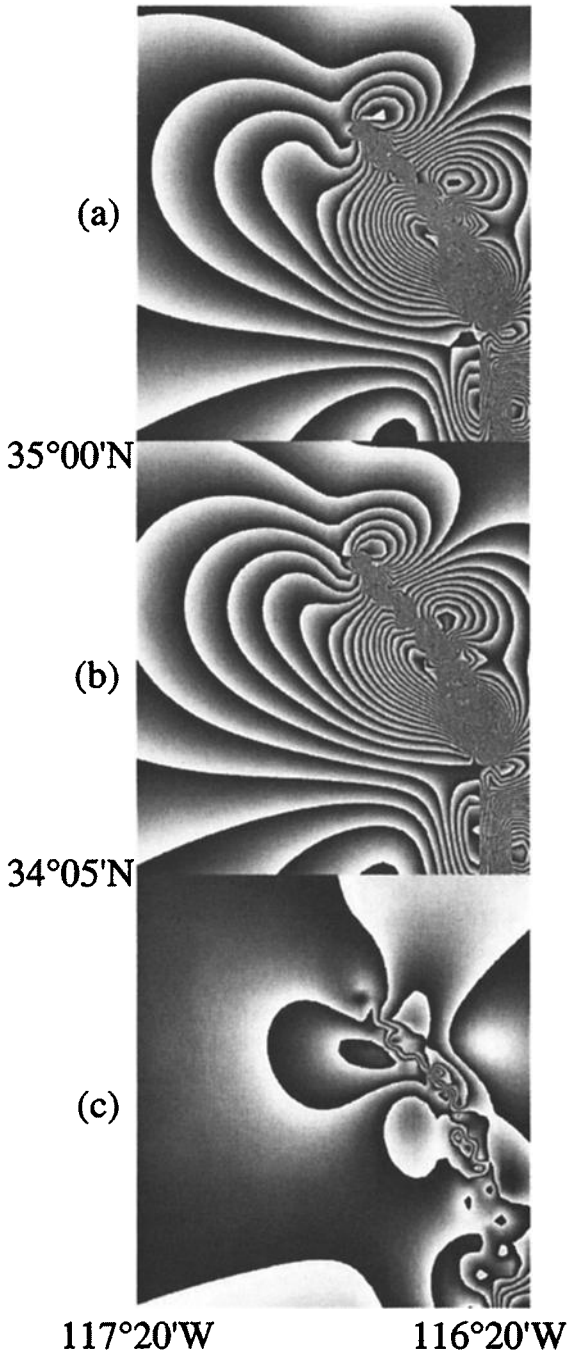

Figure 4. Misfit. (a) Interferogram constructed from the 3-asperity model (thick lines in Figure 3). (b) Synthetic interferogram produced using a model of the genetic algorithm inversion. (c) Interferogram obtained by phase subtraction of the synthetic model and of a genetic algorithm inversion solution.

results of the observations are described by a gaussian probability with expectation D and covariance matrix C_D, and that the a priori information is described by a gaussian probability with expectation m_0 and covariance C_M. We follow *Tarantola*'s [1987] formulation to calculate the model expectation

$$m = m_0 + (G^t C_D^{-1} G + C_M^{-1})^{-1} G^t C_D^{-1} (D - Gm_0) \quad (2)$$

the covariance operator on the model

$$C_{M'} = (G^t C_D^{-1} G + C_M^{-1})^{-1} \quad (3)$$

and the resolution operator.

$$R = (G^t C_D^{-1} G + C_M^{-1})^{-1} G^t C_D^{-1} G \quad (4)$$

The resolution matrix R measures how well the inverse problem can be solved with our data. The farther the resolution operator is from identity, the worse the solution is. If the diagonal element of the resolution matrix corresponding to a parameter is equal to 1, the parameter is perfectly resolved by the data set. The trace of the R matrix indicates the number of parameters effectively resolved by the data. The values of the resolution are dependent on the a priori choice of C_M and C_D. For this reason, the resolution matrix in this study is used only to compare the relative resolution of different parts of the fault or to compare results obtained with different starting models but the same data and a priori variances. A smoothing constraint is introduced through the covariance matrix C_M, which describes the a priori information on the model parameters. The values of this matrix are given by

$$C_M(i,j) = \sigma_i \sigma_j \exp\left(-\frac{1}{2}\frac{d^2(i,j)}{l^2}\right) \quad (5)$$

where l is a correlation length and d is the distance between the i^{th} and j^{th} subfaults.

Altough the least squares inversion yields a single solution with an error estimate, other solutions, perhaps within different local minima, could produce a good fit to the data. Moreover, most inversion procedures use various assumptions and restrictions that reduce the solution space, possibly excluding some reasonable solutions. For these reasons, it is necessary to explore the parameter space as extensively as possible to obtain a set of acceptable solutions. Global search methods, like the Monte Carlo technique, explore and produce multiple solutions, but become inefficient in very large parameter spaces. To solve this problem, we use a genetic algorithm [*Lomax and Snieder*, 1994] configured to find many acceptable solutions representing all regions of the model space with a good misfit. The misfit function to minimize is a L_2 norm measure of the residual difference between observed and simulated values. The slip is allowed to vary between 0 and 7 m and can take 64 different discrete values. This parameterization gives about 10^{86} possible models. Beginning with a random population of solutions, successive populations are created by selection, crossover, and mutation. The genetic algorithm produces a large set of solutions which sample the solution space globally and is particularly useful to illustrate the nonuniqueness of the solution.

5. Test With a Synthetic Simulation

We apply the inversion techniques initially to synthetic data to analyze the differences between the starting model and the solutions of the inversion. The initial three-asperity model is shown by thick lines in Figure 3. We use the same fault geometry and crustal structure for this synthetic simulation and for the actual data inversion. We compute displacement in the ground-to-satellite direction and generate a synthetic

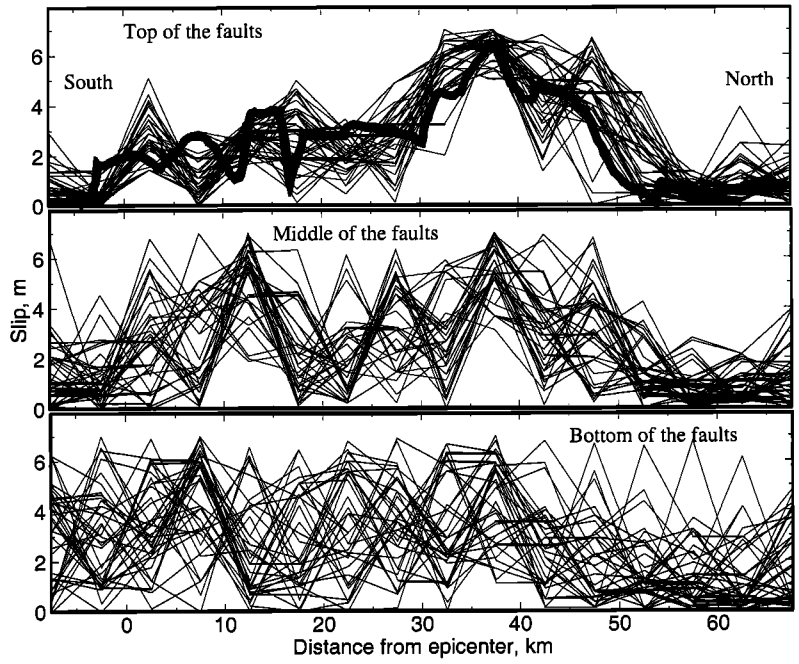

Figure 5. Results from one genetic algorithm inversion for the interferometric data points exclusively. Representative set of slip distribution on the fault. The 50 best models are plotted, and 10^5 models were tested from a model space with about 10^{30} significantly different models using a population size of 200 and 500 generations. The slip at the top of the fault is well constrained and is in agreement with geological observations (thick line). The spread of slip distribution increases with depth and spans a 3-m slip interval at the bottom of the fault.

interferogram (Figure 4). We then invert the synthetic motions in the ground to satellite direction for the same data point used for the actual SAR data. The results of the best models found by the genetic algorithm inversion are drawn in Figure 3. This synthetic test shows that the slip is well constrained in the upper part of the fault and that the resolution decreases with depth. The residual interferogram obtained by phase subtraction of the synthetic model and of the synthetic interferogram produced using an acceptable model of the genetic algorithm inversion shows residual fringes in the vicinity of the fault mostly at wavelengths shorter than our discretization of both data sampling and fault planes. With the actual data, further error can be introduced via the complexity in the fault geometry that is not modeled perfectly and the residual noise on the interferogram.

6. Application to the Landers Interferogram

In this part, we use the entire set of 406 measurements (Figure 2) of the ground-to-satellite component of the static displacement. Fifty models with the lowest misfit found with the genetic algorithm are plotted in Figure 5. The main interest of genetic inversion is that it provides a set of many acceptable solutions and then gives information about the uniqueness of the solution. It is interesting to note that even if the misfit values obtained with these 50 models are similar, the genetic inversion has found a large diversity of acceptable models. The comparison of the different models produced by the genetic algorithm gives a direct deduction of the parts of the solution that are strongly constrained by the data and the parts where parameters over a wide range are equally acceptable. The slip distribution found at the top of the fault shows a concentration of models in a range of 1 m and is in agreement with the slip measured directly by geologists in the field [*Sieh et al.*, 1993]. The models do not fit exactly the surface slip observed, especially in the southern part of the fault. This small disagreement can be explained by the fact that the slip in the model integrates the mean value for a 5-km-wide subfault, while the field measurements give information only on the superficial discontinuity. The spread of slip distribution increases with depth and spans a 4-m slip length at the bottom of the fault.

We test several correlation lengths for the least squares inversion to evaluate the effect of smoothing on the results. The solutions with various correlation lengths are represented in Figure 6. The heterogeneity pointed out in the inversion without smoothing is the same as the spatial discretization of the modeling, in particular at depth. This heterogeneity is probably not representative of the true slip at depth. It is not impossible that the slip variation could be very heterogeneous at depths but we are not yet able to test such hypothesis. Nevertheless, a smoothed solution of the least squares inversion (e.g., l=5 km) gives a good idea of the location of the main large slip areas. We note that the area of high slip at 15 km depth and 20 km north of the epicenter in Figure 6 is not real and results from an oscillatory solution. It disappears when the correlation length increases. Two main asperities appear, one located between 10 and 15 km north of the epicenter at an average depth of 8 km with a maximum slip amplitude of 5 m and a second shallower between 30 and 50 km north of the epicenter with a maximum value of around 7 m. The slip amplitude decreases to zero more than 60 km

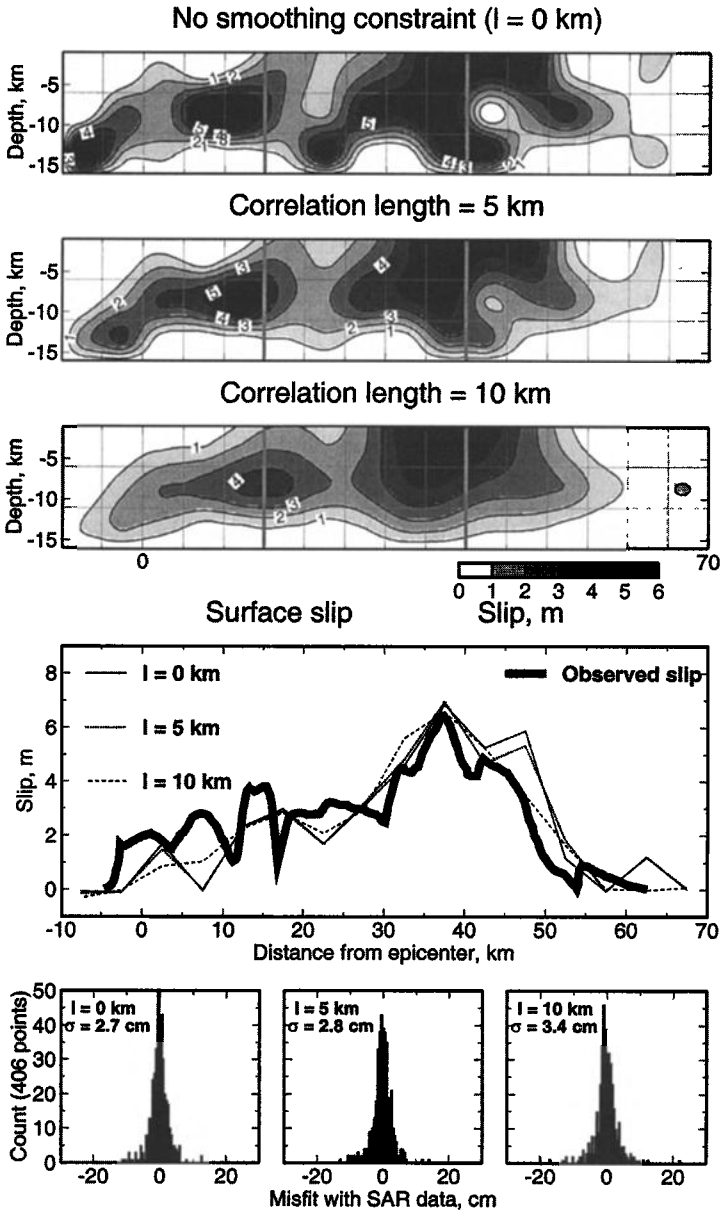

Figure 6. Cross section of the strike-slip distribution determined from least squares inversions of the SAR data points exclusively. Results with different correlation lengths are shown in the first three figures. The contour interval is 1 m, and the first contour given is 1 m. The scale bar shows the slip shading in meters. The grid represents the fault model section (northwest on left, southeast on right) displaying the subfault discretization of the three fault planes. (middle) The slip amplitude of each inversion is compared with surface measurements made on the field by geologists. (bottom) Histograms showing count as a function of the residual difference between SAR data and simulated values for the three correlation lengths.

north of the fault system. There are areas where the slip changes sign, from right lateral (as expected) to left lateral, but despite of the absence of positivity constraint, the (nonphysical) negative slip remains small. The absence of positivity constraint allows us to perform a resolution analysis that we consider to be important to achieve in inversions. The resolution of the least squares inversion, shown in Figure 7, illustrates how well the parameters are resolved with our data in different parts of the fault. This resolution decreases with depth and confirms that the slip distribution is better resolved in the upper part of the fault than at depth. The average resolution of the least squares inversion of SAR data is of the order of 84%. The residual interferogram obtained by phase subtraction of the ERS-1 observation and of the synthetic interferogram produced using the model of the least squares inversion without any smoothing constraint is drawn on Figure 8. The misfit is about 3 cm. Far from the fault the fit is very good, but the misfit increases for points near the fault where we observe two or three residual fringes. This disparity is probably due to the planar geometry assumed in our model.

7. Inversion of GPS Data

The results of the genetic inversion of the horizontal data shown in Figure 9 give a spread of the model larger than the one for SAR. The solution is not unique. The spread of slip

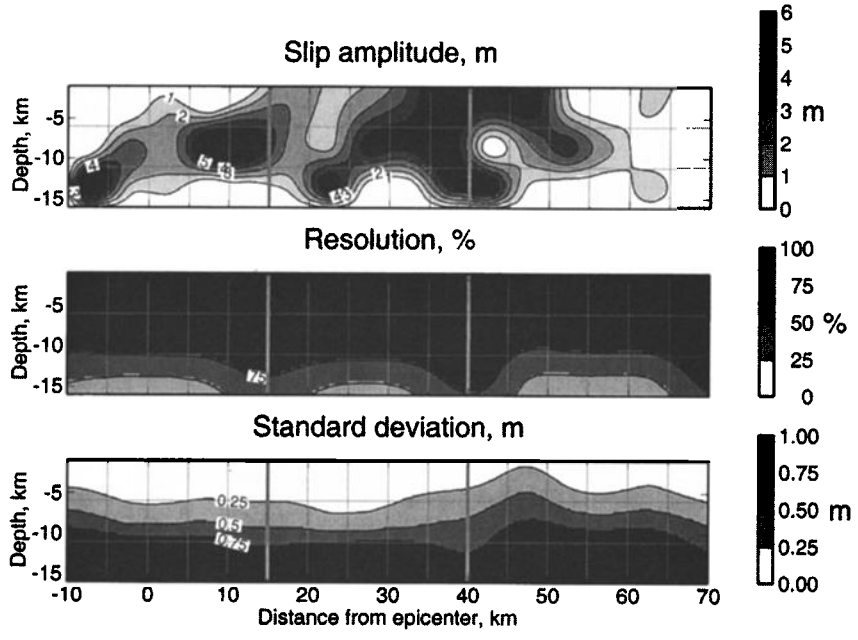

Figure 7. Cross section of the strike-slip distribution determined from least squares inversion of the SAR data points exclusively without any smoothing constraint in the inversion (top). The contour interval is 1 m, and the scale bar to the right shows the slip shading in meters. (middle) Resolution on the model parameters showing how well the parameter are resolved, the scale bar to the right shows the resolution shading in percent. The values of the resolution depend on the a priori choice of variances and allow us to compare the relative resolution of different parts of the fault. (bottom) Error estimation on the slip amplitude; the scale bar to the right shows the standard deviation on the slip amplitude shading in meters.

distribution increases with depth and spans a 5-m slip length at the bottom of the fault. The resolution of the GPS least squares inversion (Figure 10) (48%) is poorer than the resolution provided by SAR data (84%) because of the limited spatial sampling density of the available GPS stations. The imperfect modeling of the fault geometry and crustal structure also contributes to the error on the inversion results. The number of data points is too small compared with the number of slip parameters. As a result, the problem is underdetermined, and the resolution of the model is poor. This resolution decreases when the number of subfaults and consequently the number of unknowns increases. Therefore it is futile to use smaller subfaults to increase the accuracy of the estimated slip distribution. This problem of limited resolution can only be solved by adding other geodetic data. To avoid the influence of aftershocks like Big Bear or Eureka Peak, their effect could be estimated and removed from the observation as it was done by *Wald and Heaton* [1994].

The observed displacements and the ones predicted by the model resulting from the least squares inversion of the horizontal GPS data are shown by arrows in Figure 11. The fit is poor for the site located near the fault in the northern part of the earthquake. This is likely due to an inaccurate location of the fault model for the nearest station.

8. GPS and Interferogram Combined Inversion

GPS and SAR data do not cover the same time duration, but the coseismic is the predominant signal observed for both data sets [*Hernandez et al.*, 1997], we can test a joint. The modeling remains unchanged for the combined data set so that the number of unknown remains fixed while the number of data is increased. The main difficulty in this extension of the prior inversions is determining the relative weights, so that each data set is appropriately represented. A relative weighting factor, w, is introduced through the a priori covariance matrix of the data. The final values we adopted are w=1 for SAR data and w=4 for GPS data. Even with this weighting, the larger number and smaller intrinsic error of the SAR give them more influence in the inversion. The strike-slip distribution determined from SAR and GPS data combined is given in Figure 12. As expected, results of the combined inversion model are similar to those obtained using SAR data alone; the main asperities are observed in the same zones. Most of the slip occurs at shallow depth around 40 km north of the epicenter with a maximum value of around 7 m along the Homestead Valley fault. Another asperity is observed 15 km north of the hypocenter at 8 km depth.

The total resolution (Table 1) is slightly better for the joint inversion (86% without any smoothing constraint, 75% with a 5-km correlation length) than for the SAR models alone (84% and 73%, respectively). Visually, it is easy to appreciate which features in the combined dislocation model can be attributed to individual data sets. For example, in the southern part of the fault GPS have more influence due to the small number of SAR data points used in this area; the slip south of the epicentral zone is smaller in the combined inversion than with SAR data alone. We also note that in the joint inversion the slip decreases to zero at depths greater than 10 km while this was not observed with SAR data alone. GPS data improve the resolution and help to clarify the slip heterogeneity. The slip amplitude at the top of the fault is in

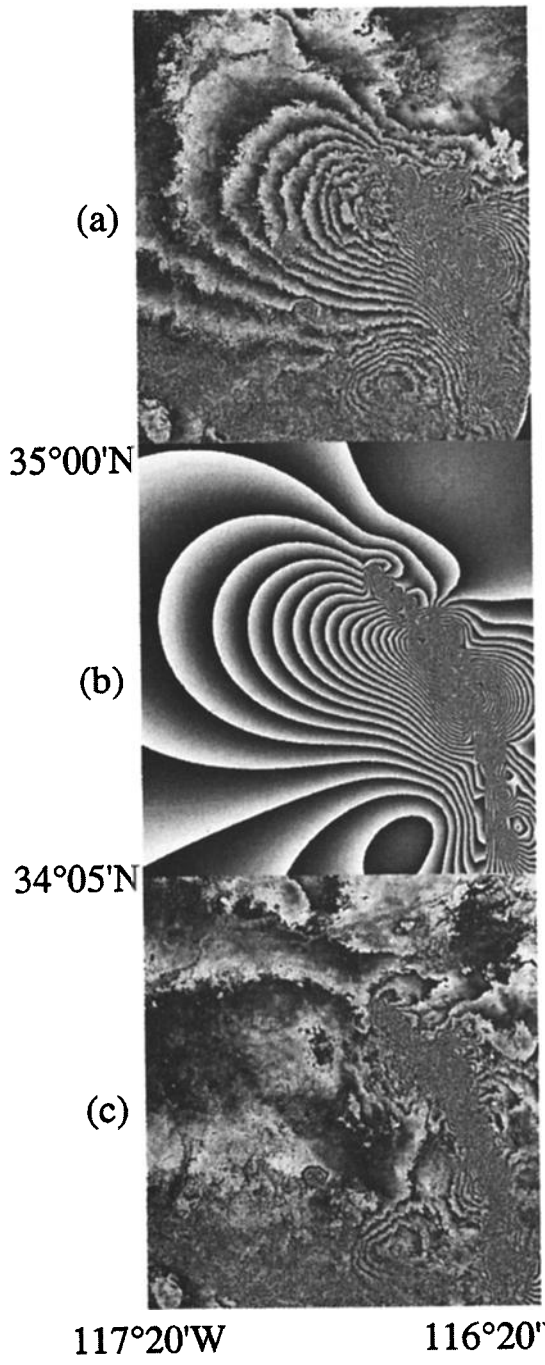

Figure 8. Misfit.(a) Interferogram constructed from two radar images acquired on April 24, 1992, and June 18, 1993. (b) Synthetic interferogram obtained with the model of the least squares inversion without any smoothing constraint. (c) Residual interferogram obtained by phase subtraction of the ERS-1 observation and of the synthetic interferogram.

agreement with geological measurements made in the field (Figure 12).

9. Strong Motion Data Inversion With Slip Distribution and Uncertainty Constrained by Geodesy

Now we have a good idea of the slip distribution and its reliability from joint inversion of SAR and GPS data using semiglobal and least squares techniques. Next, we use these results to constrain temporal variations in rupture estimated from near-field accelerograms. Our approach lies in fitting the strong ground motion data by determining the best timing associated with the slip distribution constrained by SAR and GPS joint data. We use the accelerometric data and the frequency-domain inversion procedure described by *Cotton and Campillo* [1995]. In this inversion, we estimate three source parameters: the slip amplitude, the rise time (duration of the coseismic slip on a subfault), and the rupture time (time of initiation of the rupture for each subfault). The final slip amplitude found using geodetic data is fixed through the covariance matrix of the parameters. We impose a very small standard deviation on slip parameters at the top of the fault where they are well determined by SAR and GPS. At greater depths, the slip is allowed to vary a little according to the uncertainty obtained in geodetic inversions. In contrast, the rise time and the rupture time are allowed to vary greatly by applying a large value on these temporal parameters in the a priori covariance matrix. Then we estimate the temporal parameters by inverting strong motion data using the slip distribution constrained by the results of the geodetic inversion and an a priori homogeneous rise time and a constant rupture velocity. The fit is slightly improved compared to the inversion of strong ground motion alone (Table 2 [*Cotton and Campillo*, 1995]).

This strong motion inversion in the frequency domain is nonlinear; as a consequence, the final solution depends on the parameter values of the starting model. Therefore, to explore a large domain in the solution, we compare the results with different starting models. Inversions done with various temporal initial values lead to significantly different solutions (Figure 13), while misfit are similar (Variance Reduction in Table 2). Even if the number of unknowns is reduced to the minimum using wide subfaults and constraining the slip amplitude deduced from radar interferometry and GPS measurements in the first step, significant discrepancies between final models are observed which means that the solution is not unique. The resolution of the inversions on both distance (5 km) and time (1 s) is also to take into account to assess the reliability of the result.

Although the results are scattered, the rupture front velocity is clearly variable (Figure 13). This temporal heterogeneity was not observed in previous inversions because of the trade-off between the slip amplitude and temporal parameters as well as the too-small variation of the rupture front velocity generally allowed. The best fits to the data are obtained with an initial constant rupture velocity between 2.7 and 3 km/s. Values in this range were were suggested by *Cohee and Beroza* [1994a]. The result obtained with an initial 3 km/s rupture front velocity is shown on Figure 14. In this example, the rise time and the rupture time are free to vary over a wide range around initial values of 3 s and a 3 km/s respectively. The average final rise time is of the order of 3 to 4 s. The time progression of the rupture is very heterogeneous on the fault along both the strike and dip direction. The resolution of the inversion decreases with depth. The temporal parameters are also better resolved in large slip zones.

This inversion shows a strong variation of the rupture velocity during the rupture process. At the top of the fault, where parameters are better constrained, fast rupture velocities (nearly horizontal time-distance contour in

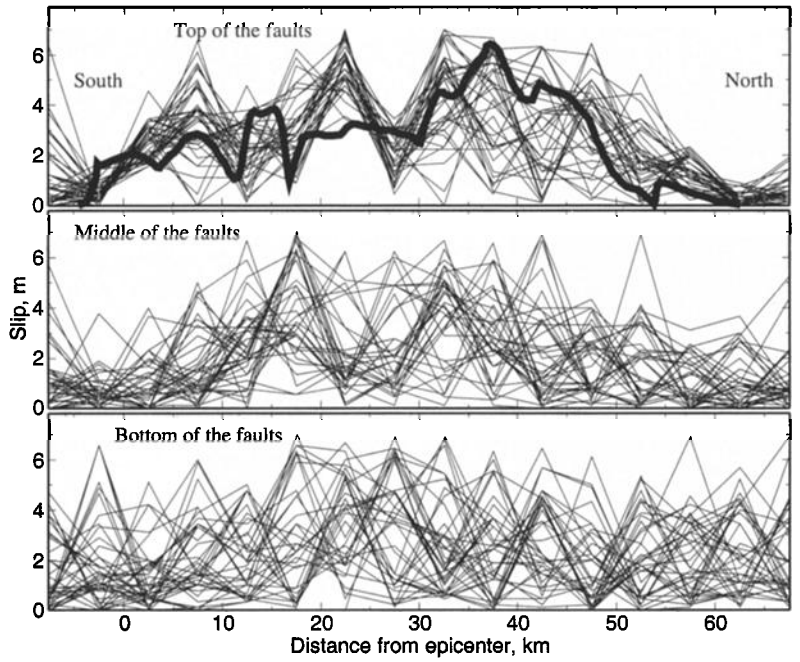

Figure 9. Results from one genetic algorithm inversion for the GPS horizontal data points exclusively. Representative set of slip distribution on the fault. The 50 best models are plotted, and 10^5 models were tested from a model space with about 10^{30} significantly different models using a population size of 200 and 500 generations. Geological observations of the surface slip are plotted in heavy line with slips solution for the subfaults located at the upper part of the fault. At the bottom of the fault, the slip is not constrained due to a lack of information in the data.

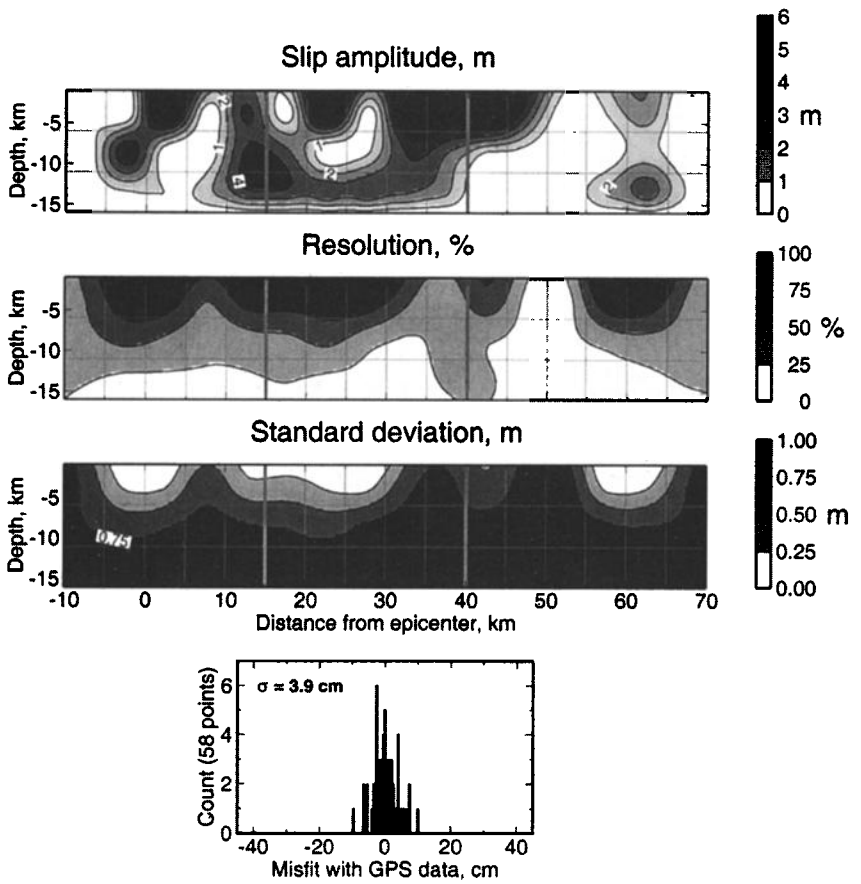

Figure 10. (top) Cross section of the strike-slip distribution determined from least squares inversion of the GPS horizontal data exclusively without any smoothing constraint in the inversion. (middle) The contour interval is 1 m, the scale bar to the right shows the slip shading in meters. Resolution on the model parameters; the scale bar to the right shows the resolution shading in percent. (bottom) Error estimation on the slip amplitude; the scale bar to the right shows the standard deviation on the slip amplitude shading in meters. Histogram showing count as a function of the residual difference between GPS measurements and simulated values.

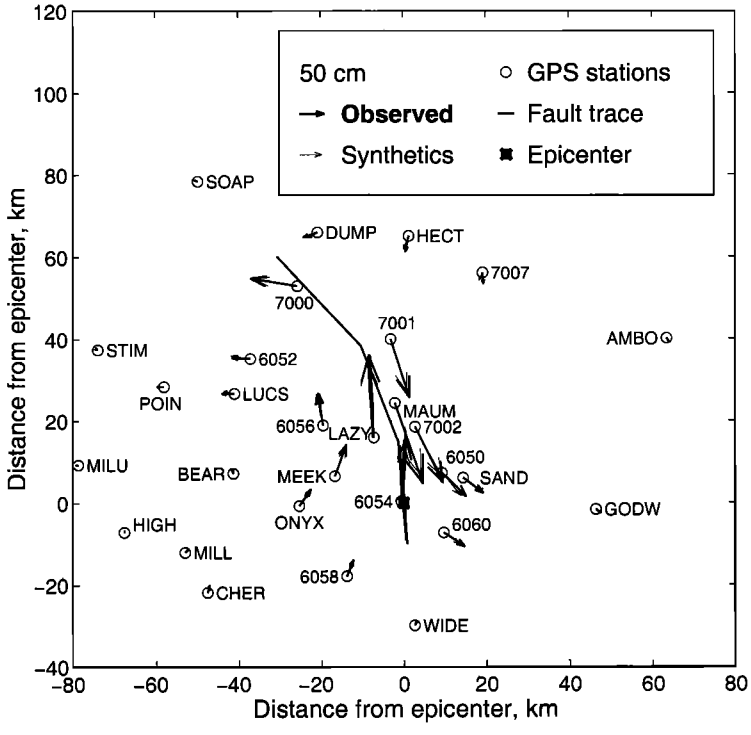

Figure 11. Location map of GPS stations used for the inversions (circle). The fault geometry used in the inversions is shown by the thin lines. The observed (thick lines) and predicted from the least squares inversion of the horizontal GPS data (thin lines) are shown by arrows, with the amplitude scaling as shown in the insert.

Figure 15) coincide with a zone of high slip. The rupture front accelerates when it encounters a high-slip zone and decreases when it encounters resistance. The rupture can either go around a resistant area (e.g., the shallow resistant area located 10 km north of the epicenter between 1.5 and 6 s in Figure 14) or restart after a barrier (a new pulse of rupture appears on the snapshot 6-7.5 s on Figure 14).

Figure 16 presents the values of the parameters found for each subfault using an initial rupture velocity of 3.0 km/s and a rise time equal to 3 s. The rupture front initiates in the southern part of the Johnson Valley fault, and its velocity increases in the middle of the first segment, where the first high-slip zone is observed. The rupture front slows as it reaches the northern limit of the Johnson Valley fault where slip transfers to the southern Homestead Valley fault. This decrease of both slip amplitude and rupture front velocity at the junction of the two faults was also observed by *Wald and Heaton* [1994]. The rupture front then accelerates again, within the shallow large slip zone located at around 40 km north of the epicenter on the Homestead Valley fault and south of the Emerson and Camp Rock faults. As far as this shallow asperity is concerned, we observe in Figure 14 that the rupture at first propagates along the edge of the asperity, starts to encircle it, and finally propagates inward. This phenomenon, best described using a well-known term of military strategy called the "double encircling pincer movement", is also observed by *Das and Kostrov* [1983] in their spontaneous rupture study of a single circular asperity. The Landers earthquake rupture finally terminates on Emerson and Camp Rock fault 20 s after initiation.

10. Discussion

The correlation between the slip amplitude and the rupture velocity is consistent with the general rupture simulation of *Day* [1982] in the presence of nonuniform prestress. Day found that in regions where the prestress is close to the yield stress, the rupture velocity is faster than the local S wave

Table 1. Inversions Reliability: Parameter Resolution and Error Estimation With Regard to Smoothing, Data Set, and Location on the Fault

Data Used	Parameters Inverted	Error Estimation on the Fault, m			Resolution and Smoothing, %		
		Surface	Middle	Bottom	l = 0 km	l = 5 km	l = 10 km
SAR	slip	1	2.5	4	84	73	47
GPS	slip	2	3.5	5	48	44	34
SAR & GPS	slip	1	2.5	4	86	75	49

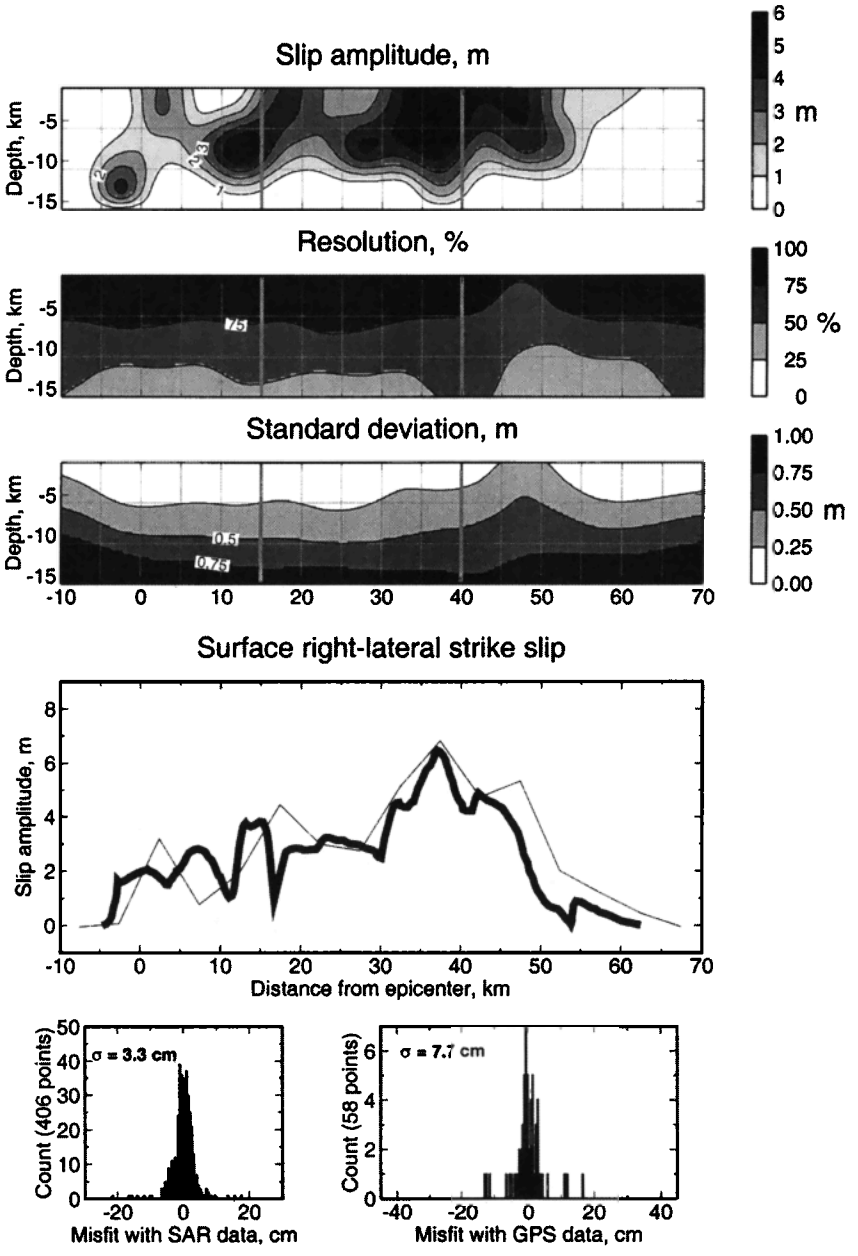

Figure 12. Cross section of the strike-slip distribution determined from GPS and SAR combined least squares inversion. The first map shows the slip distribution obtained with a 5-km correlation length. The next two images represent the spatial resolution in percent and the error estimation on the parameters, respectively. The slip amplitude is compared with surface measurements made on the field by geologists in the last graph. Histograms showing count as a function of the residual difference between observed (SAR and GPS data) and simulated values.

velocity, while in regions where the prestress is far from yield stress, the rupture velocity is slower. By analogy with Day's model, we can infer that the prestress on large slip areas was near its critical level before the main event. Strong variations of the rupture velocity are also obtained by *Olsen et al.* [1997] in their dynamic study of the Landers earthquake. From this forward modeling, they conclude that subsonic rupture velocities generally occur within and near the low-stress areas of the fault, whereas the supersonic ones dominate where the rupture resistance is relatively low. They explained the shallow supersonic rupture velocities by the free surface which promotes the generation of S to P converted head

Table 2. Kinematic Inversion. Data Fit Using Different Starting Values for the Temporal Parameters

Starting Velocity of the Rupture Front, km/s	Initial Rise Time on Each Subfault, s	Variance Reduction, %
2.5	3	70.3
3.0	3	71.1
3.5	3	69.8
3.0	2	69.5
3.0	4	70.6
3.0	5	69.3

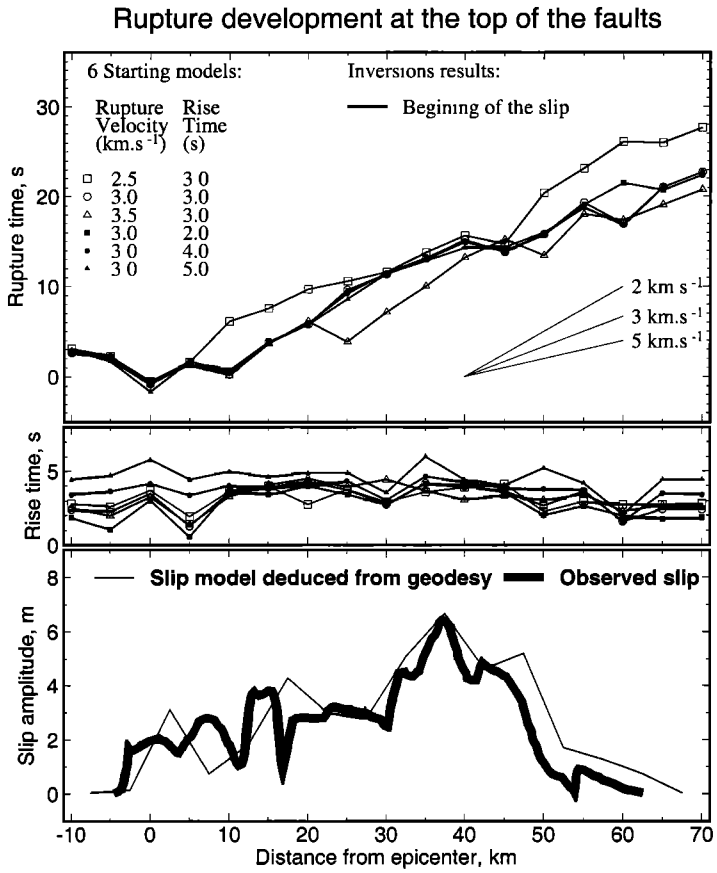

Figure 13. Final values of the (top) rupture time and the (middle) rise time for superficial subfaults obtained for six inversions with different initial temporal values. Except for the model with an initial high rupture velocity (3.5 km/s), we observe a good correlation between the rupture velocity (slope in the top graph) and the slip amplitude (bottom). The rupture front accelerates when it encounters a slip asperity and slows when a resistance occurs.

waves. *Bouchon et al.* [1998] in their stress field investigation of the Landers earthquake observe a strong spatial correlation between the local rupture front velocity and the strength excess (i.e., the difference between the static friction or the yield stress and the initial stress). Accordingly, rupture propagates at high velocity over areas of the fault where the strength excess is low and decelerates upon encountering regions where the strength excess is large. The spatial correlation we observe between the rupture velocity and the slip amplitude can be explained by the notion that an asperity probably occurs in an area with a low strength excess, where the rupture can propagate quickly without resistance. The Kickapoo fault (Figure 2) progressively transfers the 3-4 m of right lateral slip from the Johnson Valley fault to the Homestead Valley fault. North to the Kickapoo fault, the slip on the Southern Homestead Valley fault drops. The surface right slip increases farther north along a more northwesterly striking thrust fault. This part of the fault is referred to as the Homestead Valley "slip gap" because it bears a net slip deficiency relative to the 3 to 4 m of slip observed on the adjacent fault segments [*Kanamori et al.*, 1992; *Spotila and Sieh*, 1995; *Zachariasen and Sieh*, 1995]. This slip gap can be interpreted as distributed simple shear or as tilted blocks [*Peltzer et al.*, 1994]. This resistance at the beginning of the Homestead Valley fault associated with low rupture velocity can also be ascribed to the fault azimuth variation as suggested by *Bouchon et al.* [1998]. The healing of the rupture on the Emerson and Camp Rock segment is probably due to a low prestress level and to the unfavorably oriented strand of the fault, which lies at about 65° from the regional direction of the maximum compression. Nevertheless, we observe a large slip zone in the southern part of this segment and an apparent fast velocity of the rupture front that can be triggered by the dynamic stress field generated by the rupturing of adjacent fault segments as suggested by *Bouchon et al.* [1998]. Our model indicates that the slip is relatively shallow at the northern end of the rupture.

11. Conclusion

The results of SAR inversions of the Landers earthquake show that radar interferometric data alone can constrain the slip on the fault. The solution is well constrained in the upper part of the fault, while at depth the resolution is poorer, and several models with completely different characteristics can explain equally the SAR data. By using SAR data, we can constrain the asperities over the fault. The lack of resolution at depth is due to the fact that, in the case of a strike slip mechanism, the surface deformation around the fault is more sensitive to the slip near the surface than at depth. The results

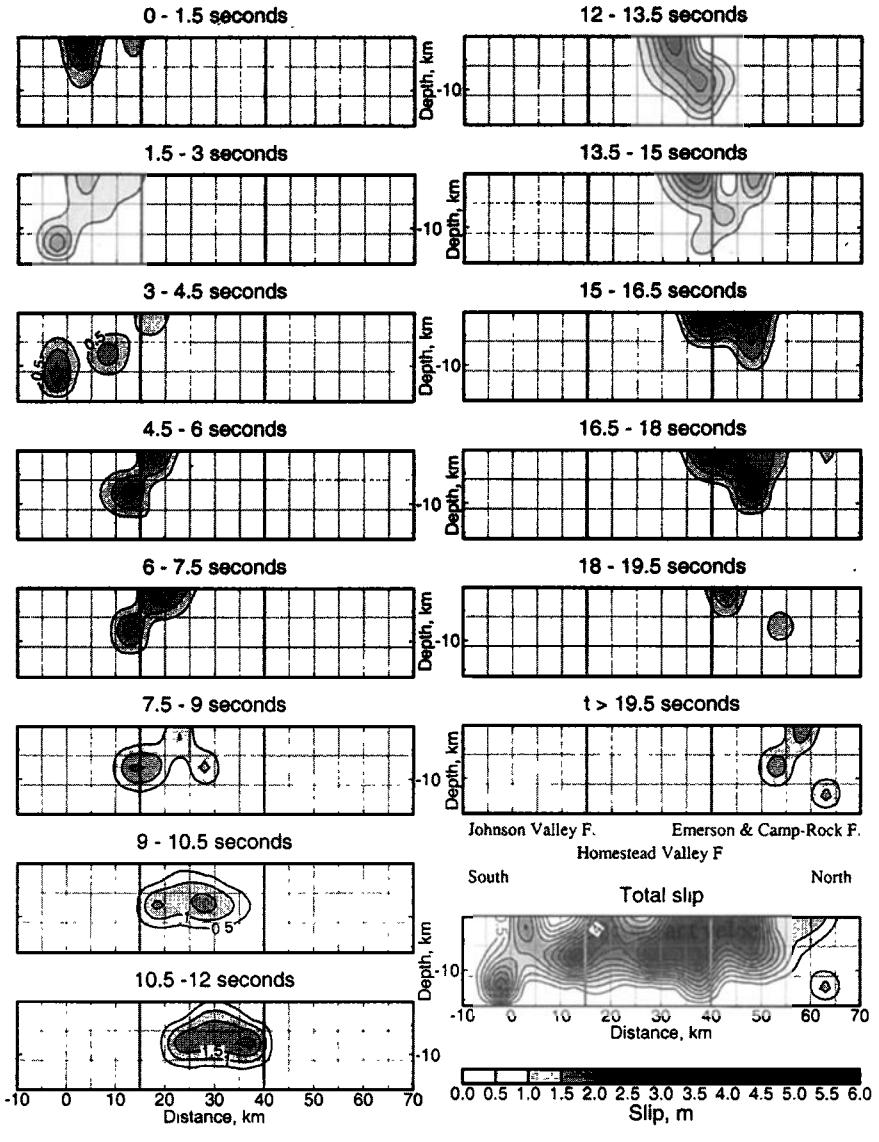

Figure 14. Time development of the Landers rupture obtained by the inversion of near field strong ground motion in the frequency domain with the a priori information on the slip amplitude determined with geodetic data. Model obtained using an initial rupture velocity of 3.0 km/s and a rise time equal to 3 s. The temporal parameters are free to vary over a wide range around an initial rise time equal to 3 s and a constant rupture front velocity (3 km/s). The rupture progression is given at intervals of 1.5 s as labeled. The contour interval is 0.5 m. The last snapshot shows the total slip distribution previously inverted with some slight modification at depth where geodesy does not constrain the slip amplitude accurately.

of the SAR inversions point out the high heterogeneity of the slip amplitude on the fault. This heterogeneity is also observed in strong motion inversions [*Cohee and Beroza*, 1994b; *Wald and Heaton*, 1994; *Cotton and Campillo*, 1995]. Our models show a good agreement with geological studies [*Sieh et al*, 1993]: the maximum surface slip occurred about 40 km north of the epicenter, with peak slip near 7 m. The slip distribution is very heterogeneous, and its variations can reach several meters over a few kilometers, but we cannot identify heterogeneities smaller than 5 km wide due to the limiting spatial discretization that we are obliged to use to make the problem well determined. In the SAR and GPS joint inversion, the total resolution is slightly increased. The error estimation on our parameters still decreases with depth, and several models with various values of slip at depth can explain the data.

The inversion of strong motion data, with the slip distribution and its error constrained by the results of the SAR and GPS combined inversion, shows a strong variation of the rupture velocity during the rupture. The rupture follows the weaker path depending on the prestress level, the fault geometry, and the dynamic process. The rupture area grows when the prestress and the fault orientation are favorable and decreases or disappears when it encounters a resistance. Some obstacles are overcome by contouring or jumping.

The large heterogeneities in both slip amplitude and rupture velocity variations suggest that the rupture propagates by breaking successive asperities rather than by propagating like a pulse at constant velocity.

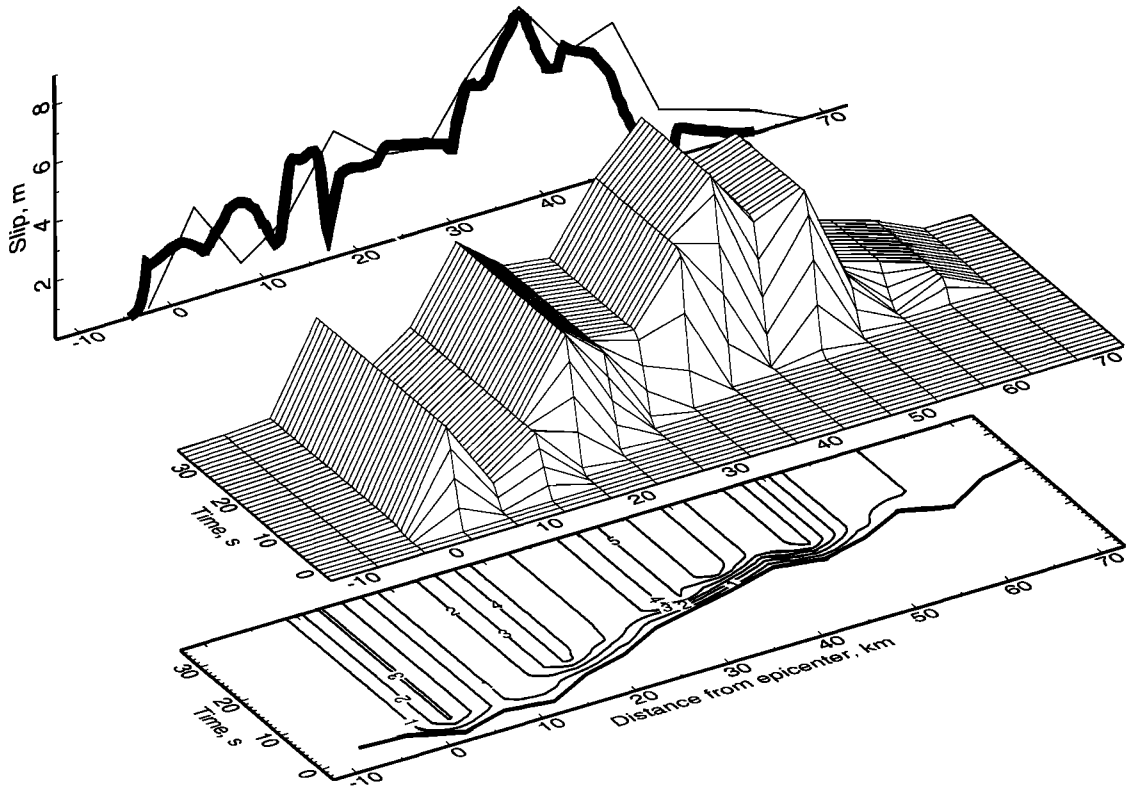

Figure 15. Model obtained using an initial rupture velocity of 3.0 km/s and a rise time equal to 3 s. three-dimentional (3-D) time-distance representation of the slip amplitude for the top subfaults. The initial rise time is equal to 3 s, and the initial rupture front velocity is constant (3 km/s). The top left 2-D graph shows the fit between the slip of the model (thin line) and the observed surface slip (thick line). The bottom 2-D graph shows the interpolated contour lines of the slip amplitude as a function of time and distance along strike direction. The thick line shows the beginning of the slip.

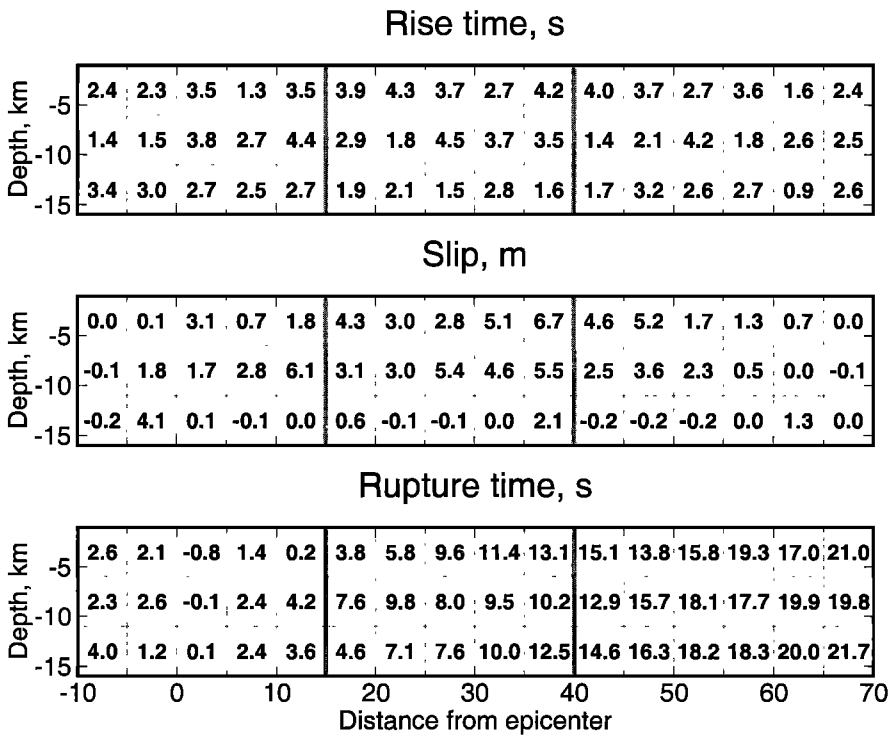

Figure 16. Values of the parameters obtained for each subfault using an initial rupture velocity of 3.0 km/s and a rise time equal to 3 s.

Acknowledgments. We are grateful to Didier Massonnet for providing a radar interferogram of the Landers earthquake. We thank Jean-Christophe Gariel who encouraged this work and Oona Scotti for helpful discussions and comments on the manuscript. The paper also benefited from the constructive reviews of Robert King, Kurt Feigl, and Raúl Madariaga.

References

Archuleta, R.J., A faulting model for the 1979 Imperial Valley, California, earthquake, *J. Geophys. Res.*, *89*, 4559-4585, 1984.

Blewitt, G., B.H. Heflin, K.J. Hurst, D.C. Jefferson, F.H. Webb, and J.F. Zumberge, Absolute far-field displacements from the 28 June 1992 Landers earthquake sequence, *Nature*, *361*, 340-342, 1993.

Bouchon, M., A simple method to calculate Green's function for layered media, *Bull. Seismol. Soc. Am.*, *71*, 959-971, 1981.

Bouchon, M., The state of stress on some faults of the San Andreas system as inferred from near-field strong motion data, *J. Geophys. Res.*, *102*, 11,731-11,744, 1997.

Bouchon, M., M. Campillo, and F. Cotton, Stress field associated with the rupture of the 1992 Landers, California, earthquake and its implications concerning the fault strength at the onset of the earthquake, *J. Geophys. Res.*, *103*, 21091-21097, 1998.

Campillo, M., and R.J. Archuleta, A rupture model for the June 28, 1992, Landers, California, earthquake, *Geophys. Res. Lett.*, *20*, 647-650, 1993.

Carlson, J.M., and J.S. Langer, Mechanical model of an earthquake fault, *Phys. Rev. A*, *40*, 6470-6484, 1989.

Cochard, A., and R. Madariaga, Dynamic faulting under rate-dependent friction., *Pure Appl. Geophys.*, *142*, 419-445, 1994.

Cohee, B.P., and G.C. Beroza, A comparison of two methods for earthquake source inversion using strong motion seismograms, *Ann. Geophys.*, *37*, 1515-1538, 1994a.

Cohee, B.P., and G.C. Beroza, Slip distribution of the 1992 Landers earthquake and its implications for earthquake source mechanism, *Bull. Seismol. Soc. Am.*, *84*, 692-712, 1994b.

Cotton, F., and M. Campillo, Application of seismogram synthesis to the study of earthquake source from strong motion records, *Ann. Geofis.*, *37*, 1539-1564, 1994.

Cotton, F., and M. Campillo, Inversion of strong ground motion in the frequency domain: Application to the 1992 Landers, California, earthquake, *J. Geophys. Res.*, *100*, 3961-3975, 1995.

Das, S., and B.V. Kostrov, Breaking of a single asperity: Rupture process and seismic radiation, *J. Geophys. Res.*, *88*, 4277-4288, 1983.

Day, S.M., Three-dimensional simulation of spontaneous rupture: The effect of nonuniform prestress, *Bull. Seismol. Soc. Am.*, *72*, 1881-1902, 1982.

Feigl, K.L., A. Sergent, and D. Jacq, Estimation of an earthquake focal mechanism from a satellite radar interferogram: Application to the December 4, 1992, Landers aftershock, *Geophys. Res. Lett.*, *22*, 1037-1048, 1995.

Fukuyama, E., and T. Mikumo, Dynamic rupture analysis: inversion for the source process of the 1990 Izu-Oshima, Japan, earthquake (*M*=6.5), *J. Geophys. Res.*, *98*, 6529-6542, 1993.

Hart, E.W., W.A. Bryant, and J.A. Treiman, Surface faulting associated wih the June 1992 Landers earthquake, California, *Calif. Geol.*, *46*, 10-16, 1993.

Hartzell, S.H., and T.H. Heaton, Inversion of strong ground motion and teleseismic waveform data for the fault rupture history of the 1979 Imperial Valley, California, earthquake, *Bull. Seismol. Soc. Am.*, *73*, 1553-1583, 1983.

Hartzell, S.H., P. Liu, and C. Mendoza, The 1994 Northridge, California, earthquake: Investigation of rupture velocity, rise time, and high-frequency radiation, *J. Geophys. Res.*, *101*, 20091-20108, 1996.

Heaton, T.H., Evidence for and implications of self-healing slip pulses in earthquake rupture, *Phys. Earth Planet. Int.*, *64*, 1-20, 1990.

Hernandez, B., F. Cotton, M. Campillo, and D. Massonnet, A comparison between short-term (coseismic) and long-term (1 year) slip for the Landers earthquake: Measurements from strong motion and SAR interferometry, *Geophys. Res. Lett.*, *24*, 1579-1582, 1997.

Hudnut, K.W., et al., Co-Seismic Displacements of the 1992 Landers Earthquake Sequence, *Bull. Seismol. Soc. Am.*, *84*, 625-645, 1994.

Ide, S., and M. Takeo, The dynamic rupture process of the 1993 Kushiro-Oki earthquake, *J. Geophys. Res.*, *101*, 5661-5675, 1996.

Kanamori, H., and G.S. Stewart, Seismological aspects of the Guatemala earthquake of February 4, 1976, *J. Geophys. Res.*, *83*, 3427-3434, 1978.

Kanamori, H., H.K. Thio, D. Dreger, E. Hauksson, and T. Heaton, Initial investigation of the Landers California earthquake of June 28, 1992, using Terrascope, *Geophys. Res. Lett.*, *19*, 2267-2270, 1992.

Kennett, B.L., and N.J. Kerry, Seismic waves in a stratified half space, *Geophys. J. Astr. Soc.*, *57*, 557-583, 1979.

Lomax, A., and R. Snieder, Finding sets of acceptable solutions with a genetic algorithm with application to surface wave group dispersion in Europe, *Geophys. Res. Lett.*, *21*, 2617-2620, 1994.

Massonnet, D., and K.L. Feigl, Radar interferometry and its application to changes in the Earth's surface, *Rev. Geophys.*, *36*, 441-500, 1998.

Massonnet, D., M. Rossi, C. Carmona, F. Adragna, G. Peltzer, K.L. Feigl, and T. Rabaute, The displacement field of the Landers earthquake mapped by radar interferometry, *Nature*, *364*, 138-142, 1993.

Massonnet, D., K.L. Feigl, M. Rossi, and F. Adragna, Radar interferometric mapping of deformation in the year after the Landers earthquake, *Nature*, *369*, 227-230, 1994.

Massonnet, D., W. Thatcher, and H. Vadon, Detection of postseismic fault-zone collapse following the Landers earthquake, *Nature*, *382*, 612-616, 1996.

Mikumo, T., K. Hirahara, and T. Miyatake, Dynamical fault rupture processes in heterogeneous media, *Tectonophysics*, *144*, 19-36, 1987.

Miyatake, T., Reconstruction of dynamic rupture process of an earthquake with constraints of kinematic parameters, *Geophys. Res. Lett.*, *19*, 349-352, 1992.

Olsen, K.B., R. Madariaga, and R.J. Archuleta, Three-dimensional dynamic simulation of the 1992 Landers earthquake, *Science*, *278*, 834-838, 1997.

Olson, A.H., and R.J. Apsel, Finite fault and inverse theory with applications to the 1979 Imperial Valley earthquake, *Bull. Seismol. Soc. Am.*, *72*, 1969-2001, 1982.

Ozawa, S., M. Murakami, S. Fujiwara, and M. Tobita, Synthetic aperture radar interferogram of the 1995 Kobe earthquake and its geodetic inversion, *Geophys. Res. Lett.*, *24*, 2327-2330, 1997.

Peltzer, G., K.W. Hudnut, and K.L. Feigl, Analysis of coseismic surface displacement gradients using radar interferometry: New insights into the Landers earthquake, *J. Geophys. Res.*, *99*, 21971-21981, 1994.

Peltzer, G., P. Rosen, F. Rogez, and K. Hudnut, Postseismic rebound in fault step-overs caused by pore fluid flow, *Science*, *273*, 1202-1204, 1996.

Quin, H., Dynamic stress drop and rupture dynamics of the October 15, 1979, Imperial Valley, California, earthquake, *Tectonophysics*, *175*, 93-117, 1990.

Savage, J.C., Displacement field for an edge dislocation in a layered half-space, *J. Geophys. Res.*, *103*, 2439-2446, 1998.

Scholz, C., *The Mechanics of Earthquake and Faulting*, Cambridge Univ. Press, New York, 1989.

Shen, Z.H., D.D. Jackson, Y. Feng, M. Cline, M. Kim, P. Fang, and Y. Bock, Postseismic deformation following the Landers earthquake, California, 28 June 1992, *Bull. Seismol. Soc. Am.*, *84*, 780-791, 1994.

Sieh, K., et al., Near field investigation of the Landers earthquake sequence, April to July 1993, *Science*, *260*, 171-176, 1993.

Spotilla, J.A., and K. Sieh, Geologic investigation of a "slip gap" in the surficial ruptures of the 1992 Landers earthquake, southern California, *J. Geophys. Res.*, *100*, 543-560, 1995.

Tarantola, A., *Inverse Problem Theory*, Elsevier, New York, 1987.

Wald, D.J., and T.H. Heaton, Spatial and temporal distribution of

slip for the 1992 Landers, California, earthquake, *Bull. Seismol. Soc. Am.*, *84*, 668-691, 1994.

Zachariasen, J., and K. Sieh, The transfer of slip between two en echelon strike-slip faults: A case study from the 1992 Landers earthquake, southern California, *J. Geophys. Res.*, *100*, 15281-15302, 1995.

B. Hernandez (corresponding author), Institut de Protection et de Sûreté Nucléaire, Département de Protection de l'Environnement, Service d'Etude et de Recherche sur la Géosphère et l'Elimination des Déchets, Bureau d'Evaluation des Risques Sismiques pour la Sûreté des Installations Nucléaires, 60-68 Avenue du Général Leclerc, B.P. 6, 92265 Fontenay-aux-Roses Cedex, France. (hernande@berlin.far.cea.fr)

F. Cotton, Institut de Protection et de Sûreté Nucléaire, Fontenay-aux-Roses, 60-68 Avenue du Général Leclerc, B.P. 6, 92265 Fontenay-aux-Roses Cedex, France. (cotton@ipsn.fr)

M. Campillo, Laboratoire de Géophysique Interne et Tectonophysique, Université Joseph Fourier, B.P. 53, 38041 Grenoble Cedex 9, France. (campillo@lgit.obs.ujf-grenoble.fr)

(Received August 24, 1998; revised January 22, 1999;
accepted February 26, 1999)